

ORIGINAL ARTICLE



Robotic posterior capsule polishing by optical coherence tomography image guidance

Matthew J. Gerber¹ | Jean-Pierre Hubschman¹ | Tsu-Chin Tsao² ¹Stein Eye Institute, University of California, Los Angeles, Los Angeles, California, USA²Mechanical and Aerospace Engineering Department, University of California, Los Angeles, Los Angeles, California, USA**Correspondence**Matthew J. Gerber, University of California, Los Angeles, Los Angeles, CA 90095, USA.
Email: gerber211@ucla.edu**Funding information**

The Hess Foundation, New York, NY, USA, Grant/Award Number: n/a; UCLA Stein Eye Institute, Grant/Award Number: n/a; National Institutes of Health, Grant/Award Numbers: R01 EY030595-01, T32-EY7026-43; Research to Prevent Blindness (RPB), New York, NY, USA, Grant/Award Number: n/a; The Earl and Doris Peterson Fund, Los Angeles, CA, USA, Grant/Award Number: n/a

Abstract**Background:** In cataract surgery, polishing of the posterior capsule (PC) can lead to improved surgical outcomes but is currently avoided due to its high-risk nature. This work developed a robotic system capable of performing PC polishing on ex vivo pig eyes using optical coherence tomography (OCT) guidance.**Methods:** The lenses of five ex vivo pig eyes were extracted and a thin layer of glue deposited onto the PC. Transpupillary OCT scans of the anterior segment were used to generate a PC-polishing trajectory. During polishing, OCT B-scans tracked the tool tip and were displayed to the operator.**Results:** Complete removal of the glue was accomplished in all five trials with no PC rupture reported.**Conclusions:** The feasibility of using a robotic system guided by OCT to perform PC polishing on a biological model was demonstrated. Contributions include modelling of the PC anatomy, intraoperative OCT visualization, and automated tool-tip motion with scheduled aspiration pressures.**KEYWORDS**

3D imaging, cataract surgery, eyes, imaged guided surgery, intraoperative imaging, mechatronics, microsurgery, minimal invasive surgery (MIS), navigation, ophthalmology, optical coherence tomography (OCT), PC polishing, posterior capsule

1 | INTRODUCTION

Cataracts are the most common cause of blindness in the world, annually affecting nearly 20 million people.¹ Cataracts are addressed through cataract surgery, a multistep procedure that involves removal of the cataract and implantation of an intraocular implant (Figure 1). The cataract is removed from the capsular bag and the posterior surface of this bag, the posterior capsule (PC), is a transparent, flexible membrane of 4–9 µm thickness.² The most frequent complication of cataract surgery is posterior capsular opacification (PCO), requiring treatment in up to 50% of patients within 3 years of cataract removal.³ The primary cause of PCO is the proliferation and migration of residual lens epithelial cells onto the posterior capsule.⁴ Nd:YAG laser posterior capsulotomy is the most frequently

performed treatment for PCO but presents vision-related complications including macular oedema, increased intraocular pressure and retinal detachment.^{5–7}

Posterior capsule polishing has been demonstrated as an effective treatment to prevent the onset of PCO and may eliminate the need for Nd:YAG laser posterior capsulotomy.⁸ PC polishing involves using an irrigation/aspiration (I/A) handpiece in close proximity to the PC and under low aspiration to clean, or “polish”, the PC anterior surface and remove the residual lens epithelial cells. Some studies have shown a statistically significant decrease in PCO rates in patients who had undergone PC polishing.^{9,10} In addition, PC polishing has been recommended in myopic eyes to reduce the risk of retinal detachment by conserving the PC in place of Nd:YAG laser posterior capsulotomy.¹¹ Therefore, if the residual lens epithelial cells can be

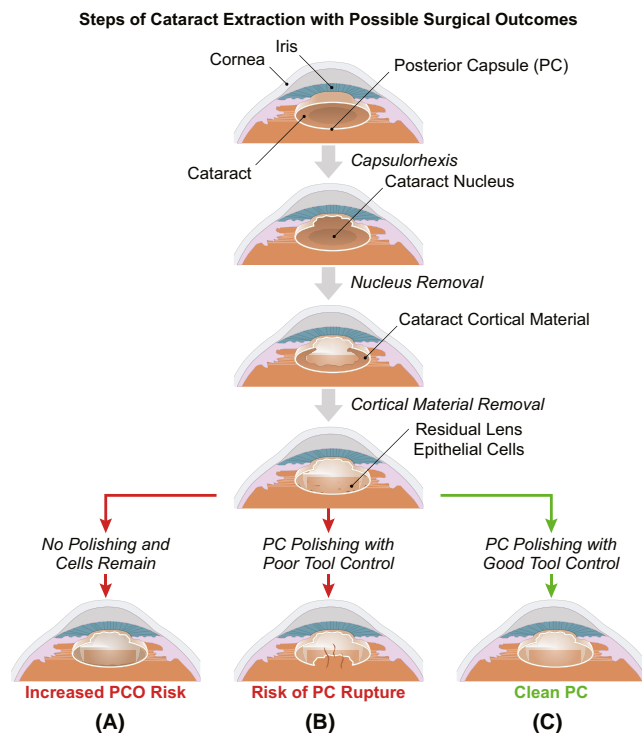


FIGURE 1 Illustration of the steps of cataract extraction with three possible surgical outcomes: (A) higher risk of PCO due to propagation and proliferation of lens epithelial cells; (B) PC rupture due to poor control of tool position and/or aspiration pressure; and (C) clean PC with decreased risk of PCO due to successful PC polishing

removed without damaging the PC or increasing surgical complications, the incidence rate of PCO can be reduced, leading to improved surgical outcomes.

However, in current practice, PC polishing is manually performed and is hindered by the physiological limitations of the human surgeon—namely limited resolution of depth sensing, poor visualization of the transparent PC and instability of the tool due to hand tremor. In fact, several studies have questioned if the increased risks of PC rupture during polishing are worth the benefits^{12–14} and many surgeons choose to skip thorough PC polishing due to the increased risk. However, accurate tool control is inherent to a robotic system and with improved sensing modalities such as optical coherence tomography (OCT), the PC can be visualized and its location known to a high degree of accuracy. By tightly integrating an OCT probe with a robotic system, PC polishing may be performed safely and effectively to alleviate the existing concerns of manually performed PC polishing, but this has, until now, never been developed or demonstrated.

In the area of intraocular robotic surgery, many of the developed systems have focused on performing vitreoretinal surgical procedures. For example, both the Preceyes Surgical System from Preceyes BV and the intraocular robotic system from the Catholic University of Leuven, Belgium have been used in teleoperation or collaborative mode to perform vitreoretinal procedures on in vivo pig eyes.^{15–17}

The Belgium group has also reported on the clinical evaluation of their system in the world's first, in-human, robot-assisted retinal vein cannulation¹⁸ and the Preceyes group has used their system to demonstrate membrane peeling in human patients.¹⁹ While both groups demonstrated success in using a robotic system to overcome the accuracy and stability requirements of delicate intraocular procedures, their use in the area of cataract surgery has not been reported. Furthermore, the field of robotic systems specifically developed for cataract surgery is limited to a handful of preliminary feasibility studies (e.g.,²⁰) and to the work of the authors using the Intraocular Robotic Interventional Surgical System (IRISS).^{21–24}

The IRISS has been used to perform teleoperated retinal vein cannulation, vitrectomy and complete lens extractions on ex vivo pig eyes.^{21,22} In addition, the IRISS has been used to demonstrate partially automated lens removal on ex vivo pig eyes with OCT feedback and minimal surgeon guidance.^{23,24} In contrast, the work presented in this paper involves performing PC polishing, which is a more challenging procedure than emulsified lens removal. To remove emulsified lens, the system can target large, floating pieces of cortical material and avoid the PC altogether by enabling a “no fly” zone. In contrast, to perform PC polishing, the system must exhibit improved control over the tool position as well as the irrigation and aspiration pressure while intentionally operating in close proximity to the delicate PC.

1.1 | Main contributions

In this paper, we report our development and demonstration of partially automated PC polishing. Innovations and contributions enabling the procedure include the following.

- Three-dimensional modelling of the PC anatomy and parameterized, automatic tool-path generation.
- Intraoperative OCT visualization of the I/A handpiece interacting with the PC during polishing for surgeon-in-the-loop feedback control.
- Robotic PC polishing by automatic tool-tip motions and scheduled aspiration pressure control.

This paper is organized as follows. Section 2 discusses the technical and surgical approaches, Section 3 shows the results of the experimental evaluation, and Section 4 discusses the significance of this work and considers future directions.

2 | MATERIALS AND METHODS

2.1 | Technical approach

The system has three relevant components: the robotic system, the OCT probe and the phacoemulsification system with an I/A handpiece and irrigation fluid reservoir (Figure 2). The robotic

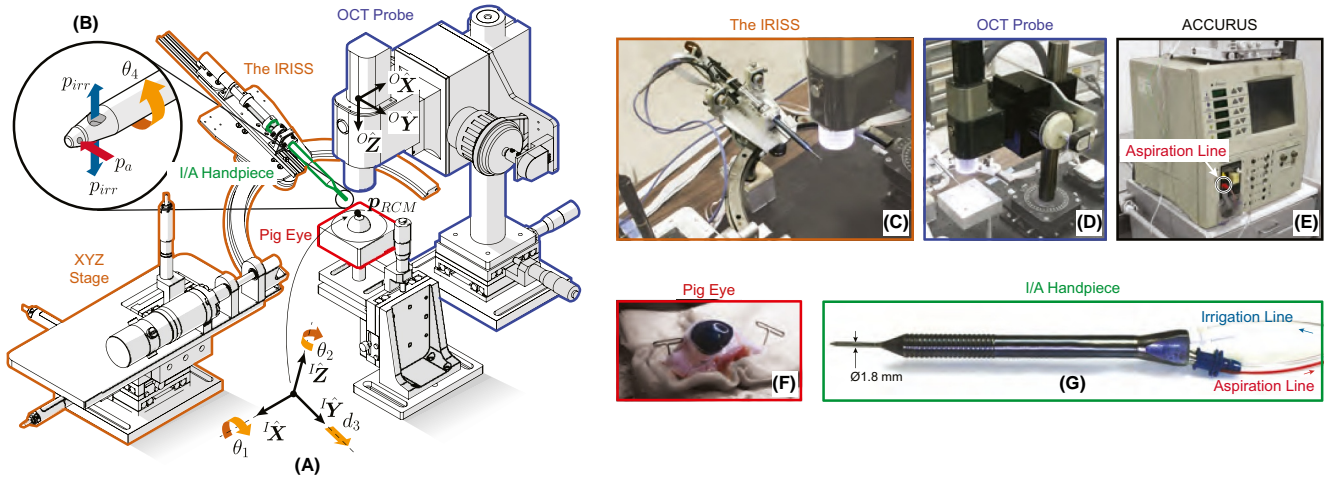


FIGURE 2 (A) Illustration of the system setup for performing PC polishing on ex vivo pig eyes. Kinematic variables are labelled. Configuration is shown with $\theta_1 = 0$, $\theta_2 = 20^\circ$ and $d_3 = -10$ mm. (B) Details of the tip of the I/A handpiece including the aspiration port which performs the polishing and the irrigation ports which maintain the fluid pressure inside the eye. Note: Polishing was performed with the aspiration port facing down (towards the PC) and is shown on the side of the tool ($\theta_4 = 90^\circ$) only for illustration. (C) Photograph of the IRISS. (D) Photograph of the OCT system. (E) Photograph of the ACCURUS used to control aspiration pressures in the I/A handpiece during PC polishing. (F) Photograph of the ex vivo pig eye model. (G) The I/A handpiece with fluid lines indicated

system used in this work was the IRISS. The IRISS is integrated with an OCT system (Telesio II 1060LR with objective lens LSM04BB; Thorlabs). The central wavelength of the system is 1060 nm, with maximum volume scan dimensions of $16 \times 16 \times 9.4$ mm and acquisition time of 33.2 s. Axial resolution is $9.18 \mu\text{m}$, lateral resolution is $25 \mu\text{m}$, with a maximum B-scan acquisition rate of approximately 12 Hz. A custom vertical mount and actuator were added to the OCT probe to enable adjustment of the scanning depth. This actuation enables a vertical translational range of approximately 40 mm and motion resolution of $1 \mu\text{m}$. For the purpose of this work, the data acquired from the OCT system was considered superior to that obtained from a standard microscope because the microscope is unable to clearly visualize the transparent membrane of the PC.

A straight-tip, I/A handpiece with a side aspiration port (8172 UltraFLOW; Alcon Laboratories, Inc.) was mounted to the IRISS. The I/A handpiece was chosen because it is currently the most common tool in practice and has been shown to obtain the cleanest capsules based on comparison with several other tool choices.²⁵ The rear aspiration port of the I/A handpiece was connected to an ACCURUS surgical system (Model 800CS; Alcon Laboratories, Inc.) to provide robot-controlled aspiration, p_a , with a maximum achievable aspiration pressure of 600 mmHg. The rear irrigation port of the I/A handpiece was connected to a bottle filled with BSS and with its fluid level a distance h above the tip of the I/A handpiece. Through physically controlling h , the irrigation pressure at the tool tip, p_{irr} can be calculated via hydrostatic pressure as $p_{irr} = \rho gh$, where ρ is the density of BSS and g is the standard gravitational constant. For this work, p_{irr} was maintained at 30 mmHg and p_a was scheduled as a function of tool-tip position relative to intraocular anatomy (Section 2), and could be overridden by operator command based on OCT feedback.

2.2 | Robot-to-OCT registration

To enable robotic guidance of the I/A handpiece using OCT feedback, the registration between the OCT reference frame, \mathcal{F}_O and the IRISS reference frame, \mathcal{F}_I , was required. The previously developed method to derive the coordinate transformation required a volume scan at 10 unique poses of the IRISS and therefore was time-consuming (upwards of seven minutes) and tedious.²³ Instead, a faster (less than 1 min) method that required only a single volume scan was developed and is described here. To begin, the IRISS was commanded to $\theta_1 = \theta_2 = 0$ and $d_3 = 9$ mm (θ_4 has no effect on tool orientation or tool-tip location). In this configuration, the tip of the I/A handpiece in the IRISS frame was ${}^I\mathbf{p}_t = [0 \ 0 \ 0]^T$ with a direction along ${}^I\hat{\mathbf{Y}}$. In addition, the I/A handpiece was within approximately 90% of the range of the volume scan, thereby maximizing the amount of tool data that could be acquired by the OCT. A volume scan was acquired and processed according to the following image-processing algorithm.

The two-dimensional matrix of raw data of each B-scan of the volume scan was converted to binary by an intensity scaling that allowed for application of a constant binary threshold. The remaining points after noise removal and morphological operations were converted to Cartesian coordinates and were added to a three-dimensional point cloud (Figure 3A). A least-squares cylinder was fit to this data using the Gauss-Newton method. The axis of the found cylinder was considered to be the centreline of the I/A handpiece and its direction defined as ${}^O\hat{\mathbf{c}}_l \in \mathbb{R}^3$. From knowledge of the relative orientation of the coordinate frames of the IRISS and the OCT probe (Figure 2), an ideal rotation from \mathcal{F}_O to \mathcal{F}_I could be defined as:

$${}^I\mathbf{R}_O = \begin{bmatrix} -1 & 0 & 0 \\ 0 & 1 & 0 \\ 0 & 0 & -1 \end{bmatrix} \quad (1)$$

which is the standard rotation by 180° about ${}^O\hat{\mathbf{Y}}$.

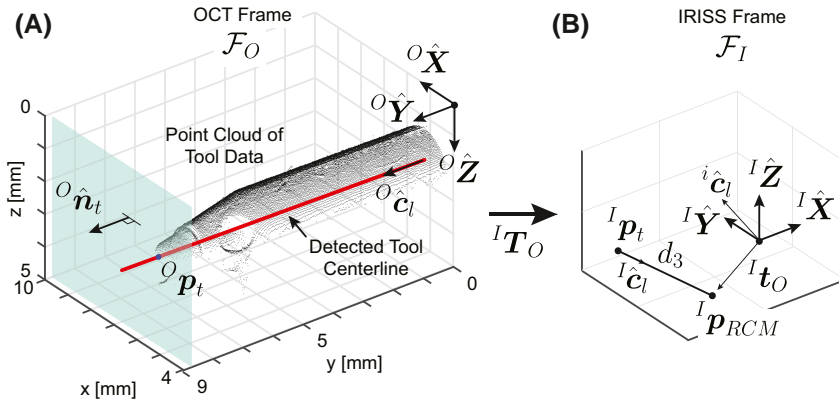


FIGURE 3 (A) Down-sampled point cloud data from an OCT volume scan with detected tool centreline (red line) shown in the OCT coordinate frame. (B) Schematic to illustrate the derivation of the OCT-to-IRISS registration and the derivation of the coordinate transformation. This registration enables the robotic system to know where the I/A handpiece is relative to the intraocular anatomy

Rotating $^O\hat{c}_l$ by iR_O resulted in $^i\hat{c}_l$, the direction of the tool centreline as if the OCT and IRISS systems were perfectly aligned. In reality, some orientation error exists and must be accounted for. The rotation matrix that transforms $^i\hat{c}_l$ into $^I\hat{Y}$ is calculated according to Equation (2) and represented as IR_i as follows:

$$^IR_i = c_\theta I_3 + s_\theta [\mathbf{u}]_\times + (1 - c_\theta)(\mathbf{u} \otimes \mathbf{u}) \quad (2)$$

$$c_\theta = \cos(\theta), \quad s_\theta = \sin(\theta) \quad (3)$$

$$\theta = \arccos(^i\hat{c}_l \cdot ^I\hat{Y}) \quad (4)$$

$$\mathbf{u} = ^i\hat{c}_l \times ^I\hat{Y} \quad (5)$$

where $I_3 \in \mathbb{R}^{3 \times 3}$ is the identity matrix, $[\mathbf{u}]_\times$ is the cross-product matrix of \mathbf{u} and \otimes is the standard outer product. In brief, Equation (2) calculates IR_i using the axis-angle representation of the rotation from $^i\hat{c}_l$ to $^I\hat{Y}$. The true rotation from \mathcal{F}_O to \mathcal{F}_I is the product of these two rotations:

$$^IR_O = ^IR_i ^iR_O \quad (6)$$

To find the translational component of the desired transformation matrix, it was necessary to first locate the tip of the I/A handpiece, $^O\mathbf{p}_t \in \mathbb{R}^3$. It was assumed that $^O\mathbf{p}_t$ will lay on $^O\hat{c}_l$ and on a plane $^O\hat{n}_t$ perpendicular to $^O\hat{c}_l$. From the OCT volume scan data, the plane between the B-scan with visible tool data near the tool tip and its closest neighbour without visible tool data near the tool tip was set as $^O\hat{n}_t$. This represents a plane perpendicular to the tool on which the tool tip resides. Therefore, $^O\mathbf{p}_t$ was calculated as the intersection between $^O\hat{n}_t$ and $^O\hat{c}_l$.

Next, $^O\mathbf{p}_t$ was rotated by IR_O to produce a point in the IRISS frame, $^I\mathbf{p}_t$. In this frame, $^I\mathbf{p}_t$ was shifted by d_3 along $^I\hat{c}_l = ^IR_O ^O\hat{c}_l$ to result in a point, $^I\mathbf{p}_{RCM}$. This is the tool-tip position as if the tool-tip had originally been at the RCM prior to the rotation. The difference between the origin of \mathcal{F}_I and $^I\mathbf{p}_{RCM}$ is the translational vector from \mathcal{F}_O to \mathcal{F}_I , $^I\mathbf{t}_O \in \mathbb{R}^3$.

With IR_O and $^I\mathbf{t}_O$ known, the homogeneous transformation matrices in this configuration were compiled as

$$^IT_O = \begin{bmatrix} ^IR_O & ^I\mathbf{t}_O \\ \mathbf{0} & 1 \end{bmatrix} \in \mathbb{R}^{4 \times 4}, \quad ^OT_I = ^IT_O^{-1} \quad (7)$$

With IT_O and its inverse known, any point in \mathcal{F}_O can be known in \mathcal{F}_I —and vice versa. This enables the IRISS to target any point within the scanning volume of the OCT system. The image-processing of the volume scan and subsequent calculation requires approximately 15 s to complete but is only performed once during system initialization. During system operation, IT_O is continually updated at a rate of 100 Hz based on known translations of the XYZ stage and OCT probe, thereby maintaining the validity of the registration despite relative motion between the hardware components. Evaluation of the registration is detailed in Appendix A and the error found to be 152.0 ± 95.9 (range: 11.5–386.2) μm . The magnitude of the error was considered acceptable because the maximum admissible deflection the PC before breakage was observed from initial experiment to be on the order of millimetres, greater than twice the maximum measured registration error.

2.3 | Eye preparation

Ex vivo pig eyes were used as the eye phantom (Sioux-Preme Packing). The unscalded eyes were from pigs butchered the previous day and shipped on ice overnight. The eyes were secured by pinning their excess flesh into a custom polystyrene holder. Preparation of each eye was performed under a surgical microscope (M840, Leica Microsystems, GmbH). A uniplanar corneal incision was created with a 2.8-mm keratome knife, followed by an 8–9 mm diameter continuous curvilinear capsulorhexis. Using BSS (NDC 0065-0800-50; Alcon), hydrodissection and hydrodelineation were performed and then the emulsified lens material was manually extracted using an I/A handpiece.

Following lens extraction, approximately 0.01 ml of water-soluble glue was extruded onto the PC using a 25-Ga, blunt-tip cannula. This glue was intended to represent residual lens epithelial cells adhered to the PC and the volume introduced was chosen by initial

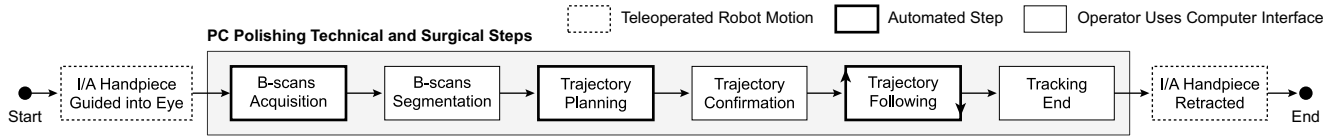


FIGURE 4 Flowchart of the procedure developed for PC polishing. This paper focuses on the contents of the grey box

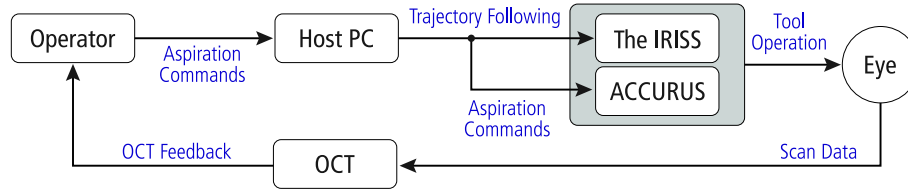


FIGURE 5 Shown is a block diagram of the system architecture during the PC polishing procedure

experiment to sufficiently cover the PC without being overly voluminous. As a final step, the anterior chamber was filled with sterile lubricating jelly (MDS032290H, Medline) to prevent collapse and maintain the capsular bag shape. The lubricating jelly has proven itself a good alternative to ophthalmic viscoelastic gel and exhibits sufficiently similar optical and material properties to those of its more expensive counterpart.

2.4 | PC polishing method

The developed procedure for PC polishing contained several major steps (Figure 4). Following preparation of the ex vivo pig eye, the eye was placed beneath the OCT probe and within the workspace of the robotic system. A pair of preoperative OCT volume scans was acquired: (1) an anterior volume scan that contained the cornea, the corneal incision, the iris and the sclera and (2) a posterior volume scan that captured a clear view of the PC. The pair of volume scans was stitched together (For the stitching, the two volume scans were combined into a single data set based on the physical translation of the probe between scans. After acquiring the first scan, the OCT probe was physically translated downwards and the second scan acquired. The second set of data was then appended to the first by a distance equivalent to the magnitude of the probe translation in the ${}^0\hat{Z}$ direction) and used for posttrial data analysis. The XYZ stage was commanded to align the I/A handpiece with the corneal incision,²³ and the I/A handpiece was guided through the cornea into the anterior chamber. Once the irrigation port of the I/A handpiece was clear of the corneal endothelium, the irrigation (30 mmHg) was engaged to maintain intraocular pressure. During the insertion, an OCT B-scan cross-section of the I/A handpiece tip was acquired and displayed to the operator at a rate of 10 Hz (Figure 5).

Once the tip of the I/A handpiece was near the posterior pole and approximately 1 mm from the PC (estimated by the operator from the intraoperative B-scan), the robot motion was paused and

nine B-scans were acquired. The B-scan planes were chosen to form an asterisk pattern with the centre near the tip of the I/A handpiece and with the scanning planes angled 20° apart. This custom B-scan pattern was chosen instead of a full volume scan because it is faster (0.8 s, cf., 33.2 s) and the specific pattern was chosen to maximize the amount of PC data available to the segmentation step. The B-scans were shown to the operator, who manually segmented all nine images by drawing a curve along the PC (Figure 6). The manual segmentation of the B-scan stack required approximately 30 s to complete per trial (Section 3).

Following the manual segmentation, each traced line was transformed to its constitute points within the three-dimensional OCT volume based on the known scan-plane location and orientation (Figure 7A). These points were first projected onto the ${}^0\hat{X}\hat{Y}$ plane (black dots in Figure 8) and a circle fit in a least-squares sense to their exterior points (blue, dotted line in Figure 8). This circle approximates the boundary of the visible PC (its diameter is roughly equivalent to that of the pupil) and it provides a boundary for the two-dimensional trajectory in ${}^0\hat{X}\hat{Y}$. A raster pattern is then generated within this circle with parameter d_p defined as the spacing between paths. For all trials, $d_p = 400\ \mu\text{m}$, which is one half the radius of the I/A handpiece.

To determine the depth of the I/A handpiece tip during the trajectory, a second-order polynomial surface was fit to the manual-segmentation points (Figure 7B). In the example shown, $R^2 = 0.90$ with residuals of $82.4 \pm 0.090\ \mu\text{m}$.

The points of the two-dimensional trajectory were then projected onto the found surface to find their ${}^0\hat{Z}$ value, thereby making the tool-tip trajectory three-dimensional (Figure 7C, red line). This trajectory was offset from the found surface by distance $d_d = 500\ \mu\text{m}$ to account for the physical size of the I/A handpiece plus the expected thickness of the glue. An example tool-tip trajectory is shown relative to the anatomy in Figure 9 for illustration purposes.

Finally, the aspiration pressure $p_a \in [p_{min}, p_{max}]$ was scheduled as a function of the tool's distance from the anatomical posterior pole. The location of the posterior pole, $p_{pp} \in \mathbb{R}^3$, was defined as the global

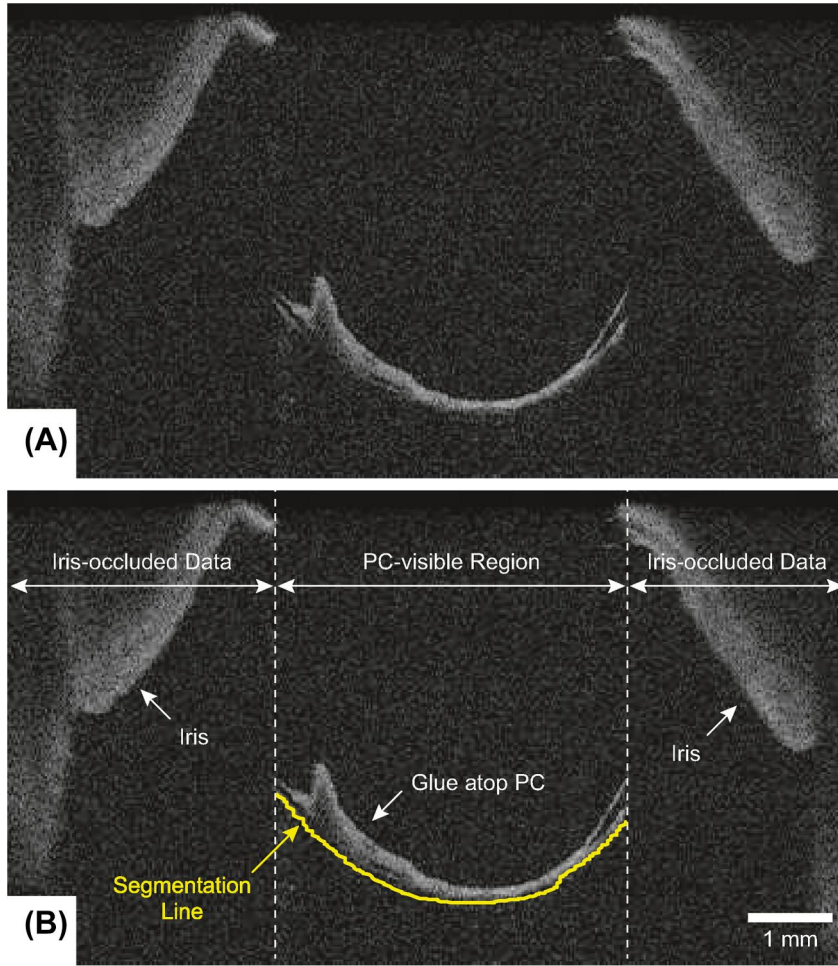


FIGURE 6 (A) An example of a single B-scan of the asterisk pattern displayed to the operator for manual segmentation of the PC location. A set of nine similarly segmented images was used to generate the tool-tip trajectory for PC polishing. (B) The same B-scan with an example of manual segmentation (yellow line) and all relevant labels

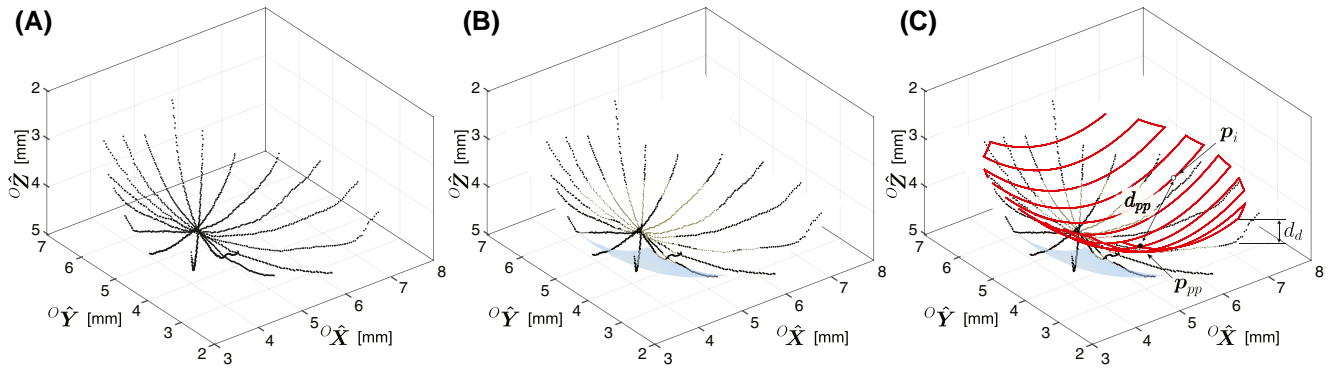


FIGURE 7 (A) The manually segmented data of the PC (black dots) from the nine B-scans reconstructed in the three-dimensional OCT volume. (B) The surface fit overlaid atop the PC and used as an estimate. (C) The generated PC-polishing trajectory (red line), offset a distance d_d from the found surface. The PC centre is defined as p_{pp} , the current location of the tool tip as the tool tracks the trajectory is defined as p_i and the scalar distance between these two points (the distance of the tool tip from the PC centre) is d_{pp} for any point on the trajectory

minimum in ${}^O\hat{Z}$ of all points on the three-dimensional trajectory. In this way, p_{pp} represents the “centre” of the PC and the furthest point from the lens equator. This point can deflect more and therefore is assumed to be the most vulnerable to breakage during polishing, although this assumption requires further analysis (Section 4). For each point $p_i \in \mathbb{R}^3$ on the trajectory, the Euclidean distance from p_i to p_{pp} is d_{pp} (Figure 7C), the distance between the tool tip and the PC

centre. The aspiration pressure was determined for each value of p_i as

$$p_a = \frac{d_{pp}}{d_{max}} (p_{max} - p_{min}) + p_{min} \quad (8)$$

where d_{max} is the distance from p_{pp} to the PC periphery. Therefore, the aspiration pressure was a linear function of the distance of the

tool-tip from p_{pp} with its minimum (p_{\min}) at p_{pp} and its maximum (p_{\max}) near the periphery of the PC.

When commanded, the IRISS tracked the tool-tip trajectory with the scheduled aspiration pressures at an average speed of

167.3 $\mu\text{m/s}$. The tracking performance was evaluated in Cartesian coordinates by a positioning error $e_t(t)$ as

$$e_t(t) = \|p_d(t) - p_i(t)\| \quad (9)$$

where $p_d(t)$ was the desired tool-tip trajectory, $p_i(t)$ was the tool-tip position measured from the encoders on each joint, and $\|\cdot\|$ is the standard Euclidean norm. Across all trials, the positioning error was 25.1 ± 17.7 (range: 0.12–52.8) μm .

Upon completion of the trajectory, the IRISS would automatically repeat the trajectory in reverse, and continue to do so until commanded by the operator to stop. For each cycle, the aspiration pressures followed those in the scheduling (Equation 8) unless overridden by the operator (Figure 10). OCT B-scans automatically tracked the location of the tool tip and were displayed to the operator at a rate of 10 Hz (Figure 11). In addition to the aspiration pressure, the operator was provided with override commands for tool position to ensure surgical safety and maintain efficacy of the PC-polishing manoeuvre. Once the trajectory was complete, a volume scan was acquired and displayed to the operator who was provided a choice to repeat the trajectory or confirm success. Upon confirmation of success, the system retracted the I/A handpiece from

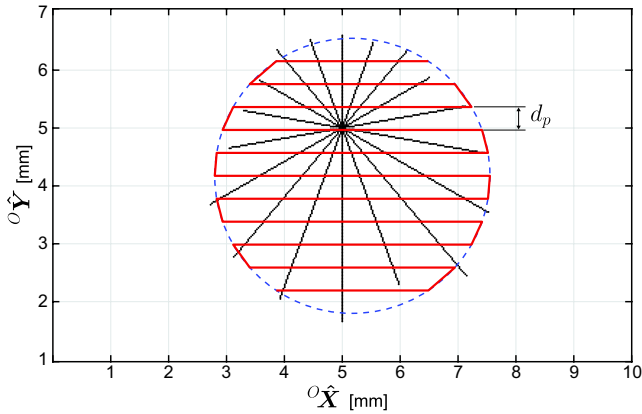


FIGURE 8 Shown is the two-dimensional raster trajectory (red line) for PC polishing. The trajectory is constrained within a circle roughly equivalent to the visible area of the PC (blue, dotted line) and is parameterized by the path spacing d_p . Black dots represent data from the manual segmentation

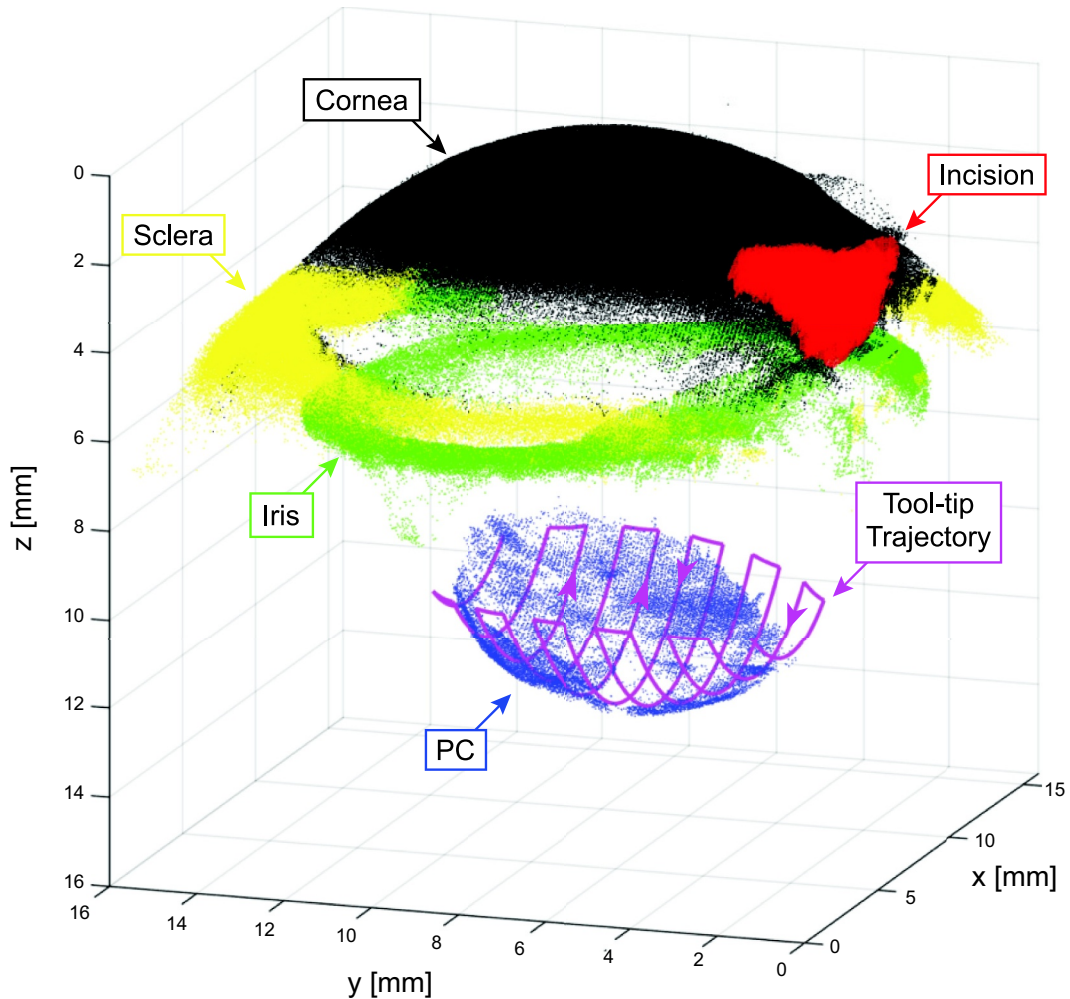


FIGURE 9 Down-sampled OCT volume scan data of the eye anatomy illustrating the system-generated trajectory for PC polishing

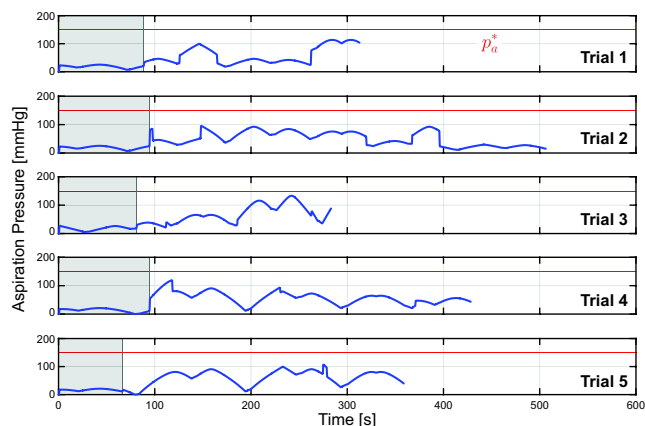


FIGURE 10 Plots showing the aspiration pressures in each trial over time. For approximately the first 60–100 s, the system tracks the scheduled aspiration pressure as a function of positioning within the anatomy (grey region), but afterwards the operator scaled the aspiration pressures based on the OCT visualization. An experimentally determined estimate of the maximum allowable aspiration pressure is shown (red line, p_a^* , Appendix B)

the eye and the procedure was considered complete. A final, post-operative volume scan was acquired for data analysis.

3 | RESULTS

Automated PC polishing was performed on $n = 5$ ex vivo pig eyes (Table 1). Analysed metrics included the total trial time, the percentage of glue removed, the number of trajectory cycles, the total travelled tool-tip distance, whether or not PC rupture occurred and the aspiration forces throughout each trial. This section discusses the results and the methods used for data acquisition and analysis.

The total trial times were calculated from timestamps automatically acquired during the procedure and defined as the time between the initial acquisition of the nine B-scans and the operator-declared trial end. By far the largest contribution to the total trial time was the duration of the PC polishing (Figure 12). The next two largest uses of time were the segmentation and trajectory confirmation by the operator, both manual processes. In comparison, the two automated steps (B-scan acquisition and trajectory planning) required negligible time.

However, due to the conservatism in both the tool speed (167.3 $\mu\text{m/s}$) as well as the aspiration pressure, the elapsed time was lengthy, several minutes longer than a human surgeon. The slow speed and low aspiration pressures were chosen with the desire to be especially careful: if the PC were to break, the surgery would need to be immediately stopped and there could be no recovery. In addition, to ensure the PC was fully clean, the cycles were allowed to repeat at least three times in every trial, which added a significant amount of time to the total duration.

The rationale for placing glue on the capsule was to demonstrate the ability of the system to clean the PC in a way that was analogous

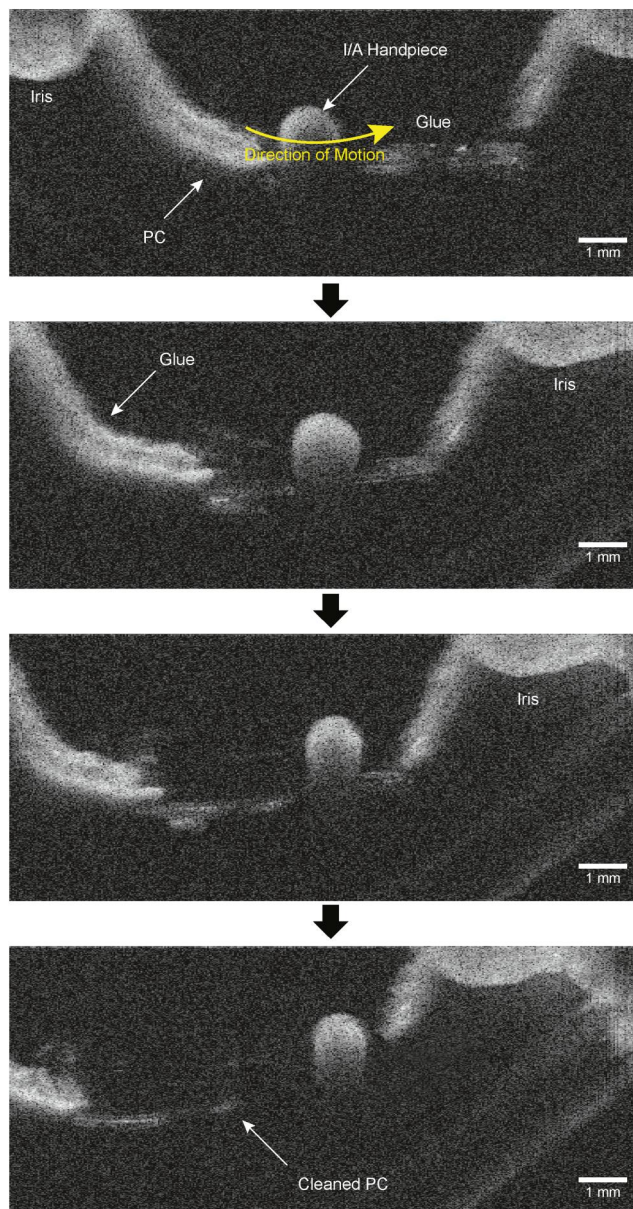


FIGURE 11 Shown is a time series of representative OCT B-scan data acquired during PC polishing that shows the I/A handpiece removing glue from the PC. These images are identical to the view the operator sees during automated polishing. The B-scans track the tool-tip location and are displayed at a rate of 10 Hz. For illustration, several intermediate frames are not shown between the frames in the figure; the elapsed time between each frame is approximately 2 s. Note that the I/A handpiece tip remains in the centre of the frame while the anatomy moves around it (the scan tracks the tip). Localized deformation of the PC occurs near the I/A handpiece due to the weak aspiration pressure

to PC polishing. To quantify the effectiveness of the cleaning, pre- and postoperative volume scans were acquired of the PC (with and without glue) and compared (Figure 13). For both volume scans, the OCT probe was moved such that the posterior pole was approximately 4 mm from the top of the scan volume to maintain similar degrees of diffusion and optical-path lengths between scans. The raw

TABLE 1 Experimental results for all five trials performed

Trial no.	Trial time	Pre-op. glue vol. (mm ³)	Post-op. glue vol. (mm ³)	Percent removal	No. of cycles	Distance travelled (mm)	PC rupture?
1	6:07	10.60	0.041	99.6	3.1	83.1	No
2	9:17	10.26	0.093	99.1	4.9	122.4	No
3	5:41	10.11	0.066	99.3	2.9	55.7	No
4	7:59	7.68	0.23	97.0	3.6	54.1	No
5	6:55	7.99	0.0043	99.9	3.0	49.2	No

Note: No PC rupture was reported in any trial.

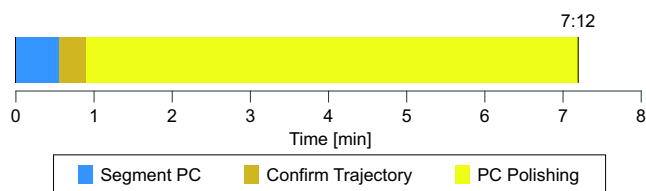


FIGURE 12 Plot showing the average required time for each procedural step. The PC polishing requires the most time followed by the two manual steps (segmentation and trajectory confirmation)

intensity data was scaled to grayscale using scaling factors that were constant between all trials and then converted to binary using a threshold value that was also constant between all trials. The entire B-scan stack was manually segmented to label all pixels that represented glue. The coordinates of the labelled pixels were used to convert the three-dimensional voxels into a physical volume ($1.47 \times 10^{-5} \text{ mm}^3$) and then multiplied by the number of voxels labelled as glue to arrive at the total volume of glue present in each volume scan. The volume of glue in the preoperative volume scan compared to the postoperative volume scan determined the percentage of glue removal. In all trials, the percentage removal was at least 97%, suggesting the system was effective at removing the glue.

As stated in Section 2, the system automatically repeated the trajectory until commanded to stop by the operator. Therefore, the number of executed cycles differed between each trial. The length of each cycle was measured as the cumulative sum of Euclidean distances between tool-tip positions at each point of the trajectory and then multiplied by the number of cycles to obtain the total trajectory length. Likewise, the time spent tracking each trajectory differed between trials: $6:18 \pm 1:32$ (range: 4:43–8:30) and the total distances travelled by the I/A handpiece were 72.9 ± 30.7 (range: 49.2–122.4) mm.

The aspiration pressures were recorded intraoperatively every 1 s of the procedure (Figure 10). For approximately the first 60–100 s of each trial, the operator allowed the system to use the scheduled aspiration pressures for polishing. This ensured minimal risk of PC rupture at the start of each trial, while the operator became familiar with the specifics of the anatomy and the PC behaviour via the intraoperative OCT feedback. After this point, and in every trial, the

operator chose to increase the aspiration pressure. Because the speed of the I/A handpiece was constant as it automatically tracked the trajectory, the operator was alleviated of all considerations other than adjusting the aspiration pressure with the goal of preventing PC rupture.

Finally, no PC rupture was reported in any of the trials. This was assessed both in analysis of the PC integrity from the postoperative OCT volume scans, as well as visual assessment through the surgical microscope at the end of each trial.

4 | DISCUSSION AND FUTURE WORK

The lack of PC rupture and the high percentage of glue removal demonstrated the ability of the robotic system to perform safe and effective PC polishing on a biological model under OCT guidance. Despite this success, there remain several areas which may benefit from future study.

During the coordinate transformation (Section 2), the accuracy of the tool-tip detection is limited by the sensing resolution of the OCT system. Aside from improvements to the OCT system itself, a B-scan located through the tool centreline could benefit from subpixel interpolation and weighting schemes, increasing the accuracy. This possibility was not investigated here, as the increase in a few microns of accuracy was considered unimportant for the studied application.

It is recognized that the overlapping nature of the B-scan pattern biases the second-order polynomial fit towards the centre where the data are denser. While the performance differences between different types of scan patterns were not investigated in this work, it remains an open area of study. Alternative scan patterns include a Lissajous pattern or others and can be evaluated based on acquisition time, percent coverage and geometric complexity. Furthermore, the number of B-scans acquired was a parameter of the scan pattern and was chosen as a trade-off between accuracy and the time requirement to acquire and manually label the scans. An in-depth analysis of this trade-off may be useful at improving the performance of the system.

In addition, the centre of the PC, p_{pp} , is the furthest point from the lens equator and can be observed to be the point of largest deflection during surgical procedures. For these reasons, it was assumed that p_{pp} would be the part of the PC most vulnerable to

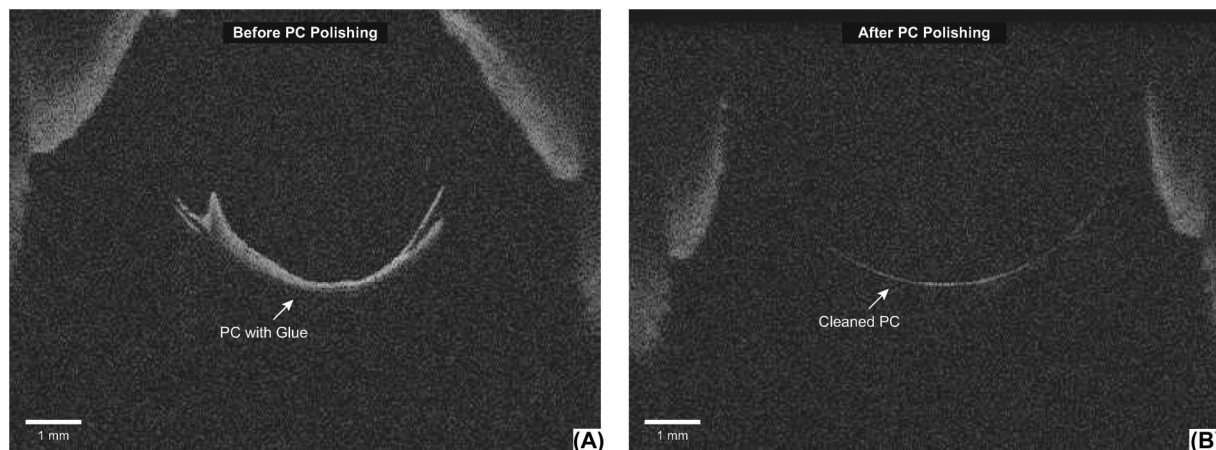


FIGURE 13 Representational B-scans acquired of the same eye at approximately the same cross-sectional plane (A) before and (B) after the automated PC-polishing procedure. *Note:* Following the preparation steps in (A), the PC is more posterior than it is following polishing in (B) because it has been forced downwards by the lubricating jelly

breakage during polishing and therefore the aspiration force was scaled down as the I/A handpiece neared this point. The assumption that the PC resiliency is a function of position must be validated through further analysis and may inform the design of future trajectories for polishing.

Future work also includes the development of automated image segmentation of the PC anatomy during the modelling step. Doing so would potentially improve the accuracy of the generated model and decrease the overall surgical time by relieving the operator of having to manually perform this step. In addition, future work can include research to conduct pressure-based control of the I/A handpiece to ensure a constant-pressure contact with the PC during polishing. Finally, the OCT-scanning speed can be increased and the operating sequence can be streamlined with feedback control of the tool motion and aspiration pressure based on PC location and shape being detected in real-time by automated image-segmentation.

5 | CONCLUSIONS

This work demonstrated the feasibility of using an intraocular robotic surgical system to perform PC polishing in ex vivo pig eyes. The significance of this work lies in both the demonstration of near-complete glue removal without PC rupture as well as in the two main innovations: (1) the ability to generate a tool-tip trajectory and schedule the aspiration pressures as a function of PC anatomy and (2) the integration of intraoperative OCT B-scans that track the tool tip and provide the operator with useful and timely intraoperative visualization during PC polishing.

In current clinical practice, many surgeons choose to skip thorough PC polishing because the increased risk of PC rupture is deemed too high to justify the benefits. However, with the incorporation of a robotic system, one of the main challenges to a human surgeon—namely physiological limitations in the control of the tool position—is avoided. In addition, in comparison to the standard

surgical microscope in use today, OCT represents a more accurate sensing modality capable of providing visualization of relevant anatomy and its relation to the surgical instrument. Through incorporation of this technology during high-risk surgical procedures such as PC polishing, the surgical risk can be decreased through improved visualization and precise, robotic guidance of the surgical instrument.

ACKNOWLEDGEMENTS

This work was supported in part by the UCLA Stein Eye Institute; The Hess Foundation, New York, NY, USA; The Earl and Doris Peterson Fund, Los Angeles, CA, USA; an unrestricted institutional grant from Research to Prevent Blindness (RPB), New York, NY, USA; unrestricted gifts that support Tsao's research program from various donors; the National Institutes of Health Grant no. R01 EY030595-01; and the Public Health Services Grant no. T32-EY7026-43.

CONFLICT OF INTEREST

The authors declare that there are no conflict of interests.

DATA AVAILABILITY STATEMENT

Data available on request from the authors. The data that support the findings of this study are available from the corresponding author upon reasonable request.

ORCID

Matthew J. Gerber  <https://orcid.org/0000-0001-9187-4827>

Tsu-Chin Tsao  <https://orcid.org/0000-0003-2087-6221>

REFERENCES

1. Pascolini D, Mariotti SP. Global estimates of visual impairment: 2010. *Br J Ophthalmol*. 2012;96:614-618.
2. Krag S, Andreassen TT. Mechanical properties of the human posterior lens capsule. *Invest Ophthalmol Vis Sci*. 2003;44:691-696.
3. Apple DJ, Solomon DD, Tetz MR, et al. Posterior capsule opacification. *Surv Ophthalmol*. 1992;37:73-116.



4. Awasthi N, Guo D, Wagner BJ. Posterior capsular opacification: a problem reduced but not yet eradicated. *Arch Ophthalmol*. 2009;127:555-562.
5. Ranta P, Tommila P, Kivelä T. Retinal breaks and detachment after neodymium: YAG laser posterior capsulotomy: five-year incidence in a prospective cohort. *J Cataract Refract Surg*. 2004;30:58-66.
6. Sakimoto S, Saito Y. Acute macular hole and retinal detachment in highly myopic eyes after neodymium: YAG laser capsulotomy. *J Cataract Refract Surg*. 2008;34:1592-1594.
7. Leydolt C, Davidovic S, Sacu S, et al. Long-term effect of 1-piece and 3-piece hydrophobic acrylic intraocular lens on posterior capsule opacification: a randomized trial. *Ophthalmology*. 2007;114:1663-1669.
8. Spalton DJ. Posterior capsular opacification after cataract surgery. *Eye*. 1999;13:489-492.
9. Paik JY, Shiloach M, Macsai-Kaplan MS. The effect of posterior capsule polishing on posterior capsule opacification. *Invest Ophthalmol Vis Sci*. 2012;53:6668.
10. Kurt A, Caglar C, Gül A, et al. Effect of anterior and posterior capsular polishing on the rate of posterior capsule opacification. *J Adv Med Med Res*. 2016;17(9):1-7.
11. Bertelmann E, Kraffel D, Hartmann C, et al. Surgical posterior capsule polishing in secondary cataract. Postoperative follow-up in 219 cases over 6 years. *Der Ophthalmologe*. 1999;96:16-19.
12. Aktan SG, Laws DE, Taylor RH, et al. Posterior capsule polishing and postoperative opacification in intercapsular cataract surgery. *European J of Implant and Refractive Surg*. 1992;4:161-163.
13. Kim KH, Sohn HJ, Song HJ, et al. Surgeon-controlled-endoillumination-guided irrigation and aspiration during combined 23-gauge sutureless vitrectomy and cataract surgery in eyes with poor fundus reflex. *J Cataract Refract Surg*. 2010;36:2028-2031.
14. Gonnermann J, Al-Mulsi S, Klamann M, et al. Long-term outcomes and complications after surgical posterior capsule polishing due to secondary cataract. *Klinische Monatsblätter für Augenheilkunde*. 2016;233:910-913.
15. Smet MD, Meenink TCM, Janssens T, et al. Robotic assisted cannulation of occluded retinal veins. *PLoS One*. 2016;11:e0162037.
16. Smet MD, Stassen JM, Meenink TCM, et al. Release of experimental retinal vein occlusions by direct intraluminal injection of ocriplasmin. *Br J Ophthalmol*. 2016;100:1742-1746.
17. Willekens K, Gijbels A, Schoevaerds L, et al. Robot-assisted retinal vein cannulation in an in vivo porcine retinal vein occlusion model. *Acta Ophthalmol*. 2017;95:270-275.
18. Gijbels A, Smits J, Schoevaerds L, et al. In-human robot-assisted retinal vein cannulation, a world first. *Ann Biomed Eng*. 2018;46:1676-1685.
19. Edwards TL, Xue K, Meenink HCM, et al. First-in-human study of the safety and viability of intraocular robotic surgery. *Nat Biomed Eng*. 2018;2:649.
20. Bourcier T, Chammas J, Becmeur PH, et al. Robot-assisted simulated cataract surgery. *J Cataract Refract Surg*. 2017;43:552-557.
21. Rahimy E, Wilson JT, Tsao TC, et al. Robot-assisted intraocular surgery: development of the IRISS and feasibility studies in an animal model. *Eye*. 2013;27:972.
22. Wilson JT, Gerber MJ, Prince SW, et al. Intraocular robotic interventional surgical system (IRISS): mechanical design, evaluation, and master-slave manipulation. *Int J Med Robot*. 2018;14:e1842.
23. Chen CW, Lee YH, Gerber MJ, et al. Intraocular robotic interventional surgical system (IRISS): semi-automated OCT-guided cataract removal. *Int J Med Robot*. 2018;14:e1949.
24. Chen CW, Francone A, Gerber MJ, et al. Semiautomated optical coherence tomography-guided robotic surgery for porcine lens removal. *J Cataract Refract Surg*. 2019;45:1665-1669.
25. Mathey C, Kohnen T, Ensikat H, et al. Polishing methods for the lens capsule: histology and scanning electron microscopy. *J Cataract Refract Surg*. 1994;20:64-69.

How to cite this article: Gerber MJ, Hubschman JP, Tsao TC. Robotic posterior capsule polishing by optical coherence tomography image guidance. *Int J Med Robot*. 2021;17:e2248. <https://doi.org/10.1002/rcs.2248>

APPENDIX A

Evaluation of Coordinate Transformation

As discussed in Section 2, two methods to obtain the coordinate-frame registration between the IRISS and OCT have been developed. The first method, Method 1, requires acquisition of volume scans at 10 unique poses of the I/A handpiece and has proven to be time-consuming and tedious.²³ Instead, an alternative method, Method 2, was developed in this work which requires only a single volume scan of the I/A handpiece. Regardless of which method is employed, a homogeneous coordinate transformation, T_m , is obtained and used the same way in the system ($m \in [1, 2]$ refers to the method number). In this section (and for notational simplicity), it is assumed T_m maps \mathcal{F}_1 to \mathcal{F}_0 , recognizing that the matrix inverse of T_m represents the inverse mapping (Equation 7).

Ideally, $T_1 = T_2$, but in general, the transformations differ due to error in the OCT data acquisition, the image processing used to detect the I/A handpiece and mechanical error of the robotic system. Because the true coordinate transformation that maps the IRISS and OCT frames is unknown, the accuracy of an obtained T_m cannot be adequately measured. However, the precision of T_m can be quantified

by obtaining T_m many times and comparing the obtained matrices according to the following method.

To quantify the precision of T_m , a set of mapped points was defined as

$$p_m^i = T_m^i p_0 \quad \forall i \in [1, n_m] \quad (10)$$

where p_m^i is a transformed point in \mathcal{F}_0 ; T_m^i is a coordinate transformation calculated by method m ; p_0 is a constant point in \mathcal{F}_1 ; and $n_1 = n_2 = 100$ are the sample sizes (the number of coordinate transformations obtained for this evaluation).

The spatial centre of all p_m^i for a particular method was calculated and defined as a reference point, p_m^* . The three-dimensional Euclidean distance between p_m^* and a value of p_m^i was defined as d_m^i , which is a measure of the difference between the obtained coordinate transformation with all others obtained by the same method. As a measure of registration error, statistical measures of all values of d_m^i were calculated (Table 2). In addition, because one of the cited justifications for developing Method 2 was to improve the speed of Method 1, the OCT data-acquisition and image-processing time requirements were also recorded and compared.

TABLE 2 Performance metric comparison

Method	Registration error (μm)
1	63.8 ± 32.2 (min: 12.0; max: 141.9)
2	152.0 ± 95.9 (min: 11.5; max: 386.2)
OCT data acquisition time (s)	
1	118.4 ± 9.7 (min: 104.1; max: 148.6)
2	34.2 ± 0.02 (min: 34.1; max: 34.3)
Image-processing time (s)	
1	146.0 ± 40.9 (min: 71.4; max: 271.0)
2	14.4 ± 1.1 (min: 9.5; max: 18.3)

The error of Method 1 is approximately half that of Method 2 (63.8, cf., 152.0), but in magnitude is still considered adequate for the PC polishing application. The main benefit of Method 2 over Method 1 is in terms of derivation time. The OCT data acquisition time is approximately 3.5 times slower from Method 1 due to the greater number of scans (10, cf., 1). Similarly, the speed of the image-processing algorithm to find the centreline of the I/A handpiece and derive the coordinate transformation benefits from fewer scans, as Method 2 is approximately 10 times faster than Method 1.

APPENDIX B

Maximum Allowable Aspiration Pressure

To determine the maximum allowable aspiration pressure that would result in PC rupture, p_a^* , three pig eyes were prepared by the process outlined in Section 2. The I/A handpiece was positioned 500 μm above the PC at its centre with the aspiration port facing downwards.

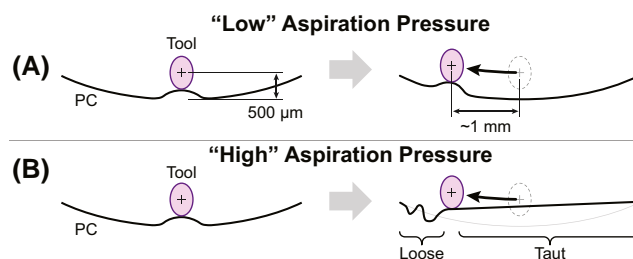


FIGURE 14 Illustrations of the experimental evaluation to determine the maximum allowable aspiration pressure that would result in PC rupture, p_a^* . (A) The trial executed with non-zero, “low” aspiration pressure. (B) The trial executed with “high” aspiration pressure. *Note:* The left-hand side of (A) and (B) are nearly indistinguishable, necessitating the tool movement to enact a detectable change in PC shape

In this position, the aspiration pressure was set to a constant value and the robot was commanded to move the I/A handpiece approximately 1 mm along the PC (Figure 14). The effect on the PC from this motion was recorded in the OCT B-scan. The aspiration pressure was then incremented higher and the trial repeated.

Two states could be observed for the PC shape recorded in the OCT data: at lower aspiration pressures, the PC locally deforms near the tip (Figure 14A); at higher aspiration pressures, the PC stretches opposite the direction of motion (Figure 14B). The values of aspiration pressure that transitioned between these two states that were observed for the three pig eyes were 150, 222, and 240 mmHg. It is expected that aspiration pressures greater than these values would increase the risk of PC rupture and should be avoided. The minimum of these three values (150 mmHg) was used as the value of p_a^* shown in Figure 10.